Carbon Trends 13 (2023) 100300

Contents lists available at ScienceDirect

Carbon Trends

journal homepage: www.elsevier.com/locate/cartre

Impact of material and tunnel barrier quality on spin transport in a CVD graphene non-local spin valve device array

Samuel T. Olson, Daniel Still, Kaleb Hood, Otto Zietz, Jun Jiao *

Department of Mechanical and Materials Engineering, Portland State University, 1930 SW 4th Ave, Portland, OR 97201, USA

ARTICLE INFO

Keywords:
Spintronics
Graphene
Non-local spin valve
Raman spectroscopy

ABSTRACT

Wafer-scale graphene films produced via chemical vapor deposition (CVD) are now commercially available, however these films inherently contain randomly distributed defects such as adlayers and grain boundaries. This report discusses the impact of these defects on the signal integrity of an array of graphene-based non-local spin valves (NLSVs). It was found that critical spin parameters fluctuate drastically between adjacent identical devices. Investigation of the channel quality indicated that adlayers do not affect spin signal significantly even when located directly in the spin transport region of the device. In contrast, grain boundary defects within the spin transport region have significant impact on spin signal. Poor tunnel barrier integrity due to residue from the fabrication process also remains a dominant factor driving device variability.

1. Introduction

The field of spintronics involves the study of devices that store and manipulate information based on the spin of electrons rather than their charge. The focus on electron spin instead of charge has the potential to produce logic devices that consume minimal power and operate at very high frequencies [1–3]. Lateral spin valves, which serve as tools for measuring spin transport properties of a material, are simple spintronic devices that consist of a pair of ferromagnetic electrodes of differing widths separated by a non-magnetic channel [4,5]. An external magnetic field is applied parallel to the electrodes, and the resistance between the electrodes changes when their magnetic polarizations are antiparallel due to an effect known as giant magnetoresistance (GMR) [6]. In the local spin valve (LSV) configuration, only two electrodes are used – a continuous current is injected between the two electrodes, and the voltage is measured across them. The local resistance (R_L) is then trivially calculated using Ohm's law ($R_L = V/I_{inj}$). In contrast, the non-local spin valve (NLSV) consists of four electrodes – two adjacent electrodes are used as the current injection loop, while the other two electrodes detect a non-local voltage that arises due to a spin imbalance from the spin-polarized current injected via the injection loop [7]. With the detection electrodes lying outside the charge injection loop, the charge current and spin-polarized current can be separated, increasing the signal-to-noise ratio of the spin signal. The non-local resistance (R_{NL}) is again calculated using Ohm's law as $R_{NL} = V_{det}/I_{inj}$. The spin signal (ΔR_{NL}) is defined as the difference in resistance between the parallel and antiparallel states of the electrodes. As the detected voltage (and correspondingly, ΔR_{NL}) is proportional to the spin-polarized accumulation underneath the detector electrode, spin scattering in the channel region between the injector and detector electrodes is expected to reduce the resulting spin signal [8,9].

Graphene consists of a single atomic layer of sp^2-bonded carbon atoms arranged in a two-dimensional honeycomb lattice. Theoretical and experimental investigations have shown that graphene has unique electronic properties that make it capable of serving as a channel material for spintronic applications [10–14]. Many studies employ single NLSV devices fabricated on a pristine mechanically exfoliated graphene sheet, which is inherently unscalable. Since its initial isolation from graphite via mechanical exfoliation in 2004 [15], there has been a large effort devoted to developing methods for controlled fabrication of wafer-scale monolayer graphene, most often employing chemical vapor deposition (CVD) [16–20]. CVD fabrication of graphene involves flowing carbon-containing gases (e.g., methane or acetylene) into a vacuum chamber at high temperature (>900 °C), where they interact with a transition metal catalyst (e.g., Ni or Cu) resulting in surface coverage of graphene. The resulting graphene can then be transferred onto an arbitrary substrate [21].

Although the CVD process greatly facilitates the fabrication of wafer-scale monolayer graphene, it is not without its faults. Due to the nucleation-outgrowth process of growth on the metal catalyst, grain

* Corresponding author.
E-mail address: jiaoj@pdx.edu (J. Jiao).

https://doi.org/10.1016/j.cartre.2023.100300
Received 28 September 2023; Accepted 29 September 2023
Available online 29 September 2023

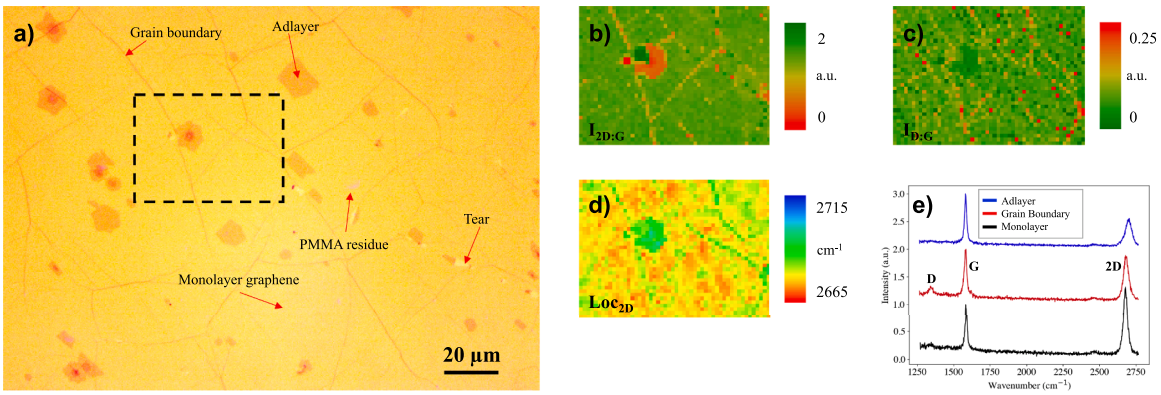

Fig. 1. (a) Optical micrograph of bulk graphene surface, showing various adlayers, grain boundaries, and other features in the graphene sheet, (b) 2D:G intensity ratio, (c) D:G intensity ratio, and (d) 2D peak location Raman maps of the area outlined by the dashed box in (a). (e) Characteristic Raman spectra from monolayer, grain boundary, and adlayer regions.

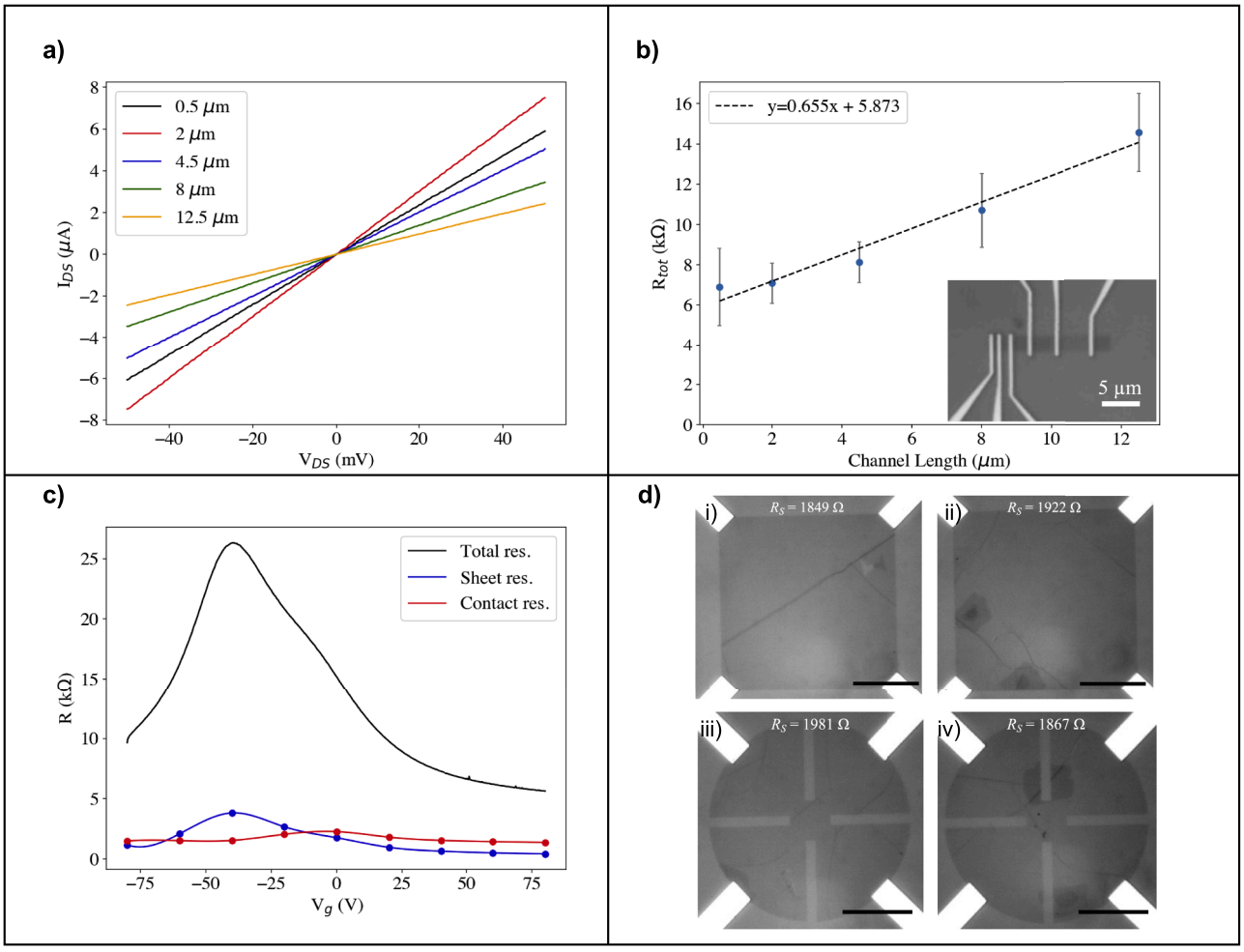

Fig. 2. (a) I-V curves for a single graphene TLM device with channel separations varying from 0.5 to 12.5 µm. (b) Total resistance versus channel length averaged over five devices, error bars represent standard deviations. *Inset*: optical micrograph of a representative graphene TLM device. (c) Total, sheet, and contact resistance versus gate voltage. (d) Van der Pauw squares (i, ii) and clovers (iii, iv) with various defects, sheet resistance measurements (R_S) overlayed. Scale bars indicate 15 µm.

boundaries and adlayers (additional layers on top of the monolayer) tend to develop in the films [22–24]. Additionally, the transfer process from the metal catalyst to an arbitrary substrate (typically Si/SiO_2) introduces additional defects into the films such as tears, folds, and PMMA residue [25–27]. The presence of these defects results in a graphene film that is inhomogeneous across its surface, which has potential implications for the wafer-scale fabrication of graphene-based electronic devices. Grain boundaries are known to be a noise source [28], and a source of increased carrier scattering which can be impacted by an external magnetic field [29]. Multilayer graphene tends to have higher resistance than monolayer graphene and introduces differences in the electronic band structure [30,31]. PMMA residue on the surface of

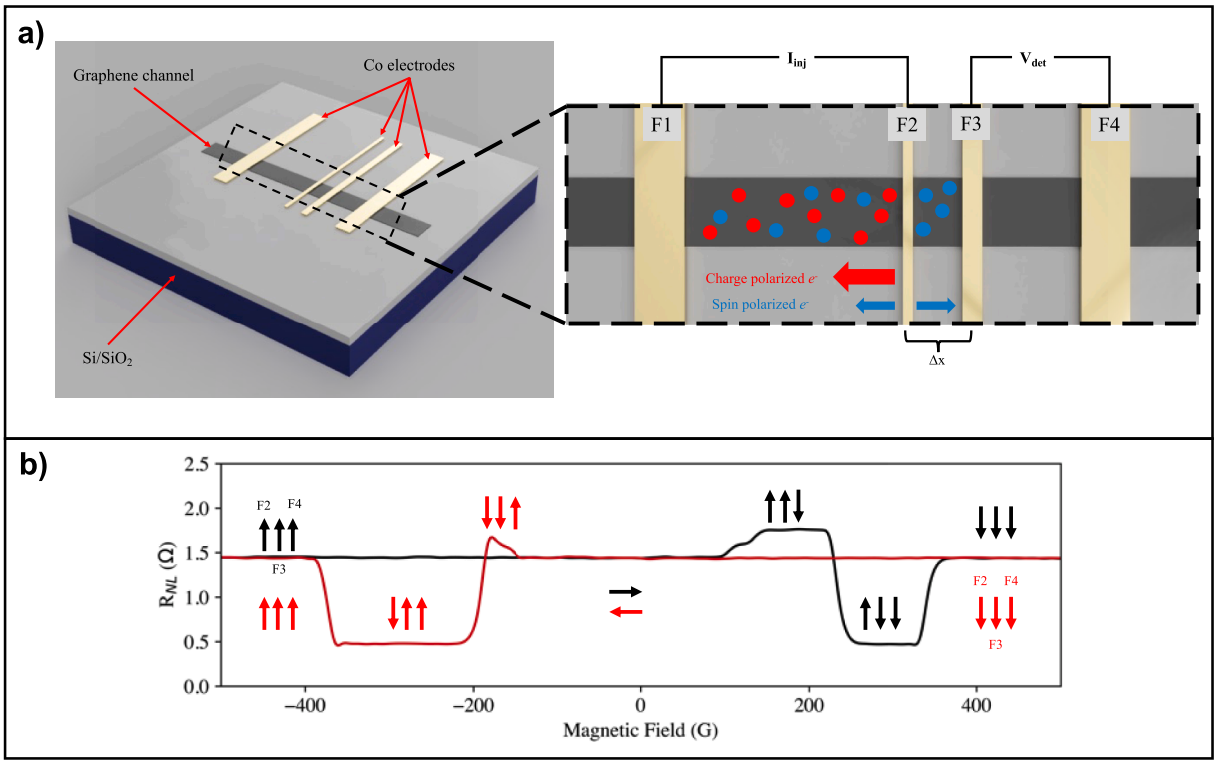

Fig. 3. (a) Model representation of standard non-local spin valve geometry, with current ground electrode (F1), current injector electrode (F2), detector electrode (F3), and detector reference electrode (F4). Current is injected between electrodes F1 and F2, and the non-local voltage is recorded between electrodes F3 and F4. The injector and detector electrodes (F2 and F3) are separated by a distance Δx. Red circles represent charge-polarized electrons, blue circles represent spin-polarized electrons. (b) An example of a non-local resistance versus magnetic field sweep, polarizations of each participating electrode are indicated by the vertical arrows. Black lines indicate forward sweeps (increasing magnetic field), and red lines indicate reverse sweeps (decreasing magnetic field).

Table 1
Median, maximum, minimum, and standard deviation of device characteristics for 1 μm ($N = 9$) and 2 μm ($N = 6$) devices.

	$\Delta x = 1$um				$\Delta x = 2$um			
	Med.	**Max.**	**Min.**	**S.D.**	**Med.**	**Max.**	**Min.**	**S.D.**
ΔR_{NL} (Ω)	0.94	5.249	0.81	1.522	0.975	1.36	0.27	0.434
Phase (deg)	21.6	96.1	1.18	33.7	15.9	18	8.67	3.31
Dirac Point (V)	−33.8	−31.2	−38.2	1.93	−35.8	−26.4	−37.6	4.34

graphene is known to cause light p-type doping and reduced carrier mobility, in addition to increased contact resistance [32–34]. Tears and folds in the graphene sheet can destroy the integrity of the channel outright.

To understand the effects of these inhomogeneities on the performance of graphene-based spintronic devices, we fabricated an array of graphene NLSVs on commercially available CVD-grown graphene. The graphene is first characterized using optical microscopy and Raman spectroscopy to establish a baseline for its spatial defect distribution. Non-local resistance measurements are then taken in a varying magnetic field to determine the spin signal and contact quality of each device. The device channels are subsequently analyzed using Raman mapping to observe the distribution of defects present in the graphene. The findings characterized by this systematic investigation are discussed in the following report.

2. Materials and methods

2.1. Device fabrication

The NLSV devices are fabricated from commercially available CVD-grown graphene on 100 mm p-type doped Si wafers with a 285 nm oxide layer (Grolltex Inc). Graphene channels are defined using electron beam lithography (EBL) followed by a standard O_2 etching method at 50 W of power for 60 s at a chamber pressure of ~5 mTorr. The channels are 1.4 μm wide and 16 μm long from end-to-end. After the graphene channel etching was complete, the 100 mm wafer was diced into 16 individual arrays each containing 20 NLSVs, as well as other electronic test structures. EBL was again used to pattern the electrode layer. The injector and detector electrodes that are used to manipulate spin signals in the devices were designed to have different widths (200 nm and 400 nm respectively) to ensure different magnetic susceptibilities during sweeping. The injector ground and detector reference are both 1 μm in width. All four electrodes consist of 25 nm thick electron beam evaporated Co (see Fig. 3a below). The Co electrodes are separated from the graphene channel by a 1.5 nm TiO_2 layer, which acts as a tunnel barrier for reducing spin backflow into the electrode due to the impedance mismatch between Co and graphene [12,14,35]. The TiO_2 layer was fabricated in two identical back-to-back processes, consisting of depositing 0.75 nm of Ti via electron beam evaporation followed by *in situ* oxidation at 1 Torr in a pure O_2 atmosphere for 15 min. Both the e-beam deposition and *in situ* oxidation were performed in a KJL AXXIS physical vapor deposition system. Lift-off for each process step was accomplished in warm acetone. A final vacuum annealing step at 300 °C for two hours was conducted after lift-off of the final layer.

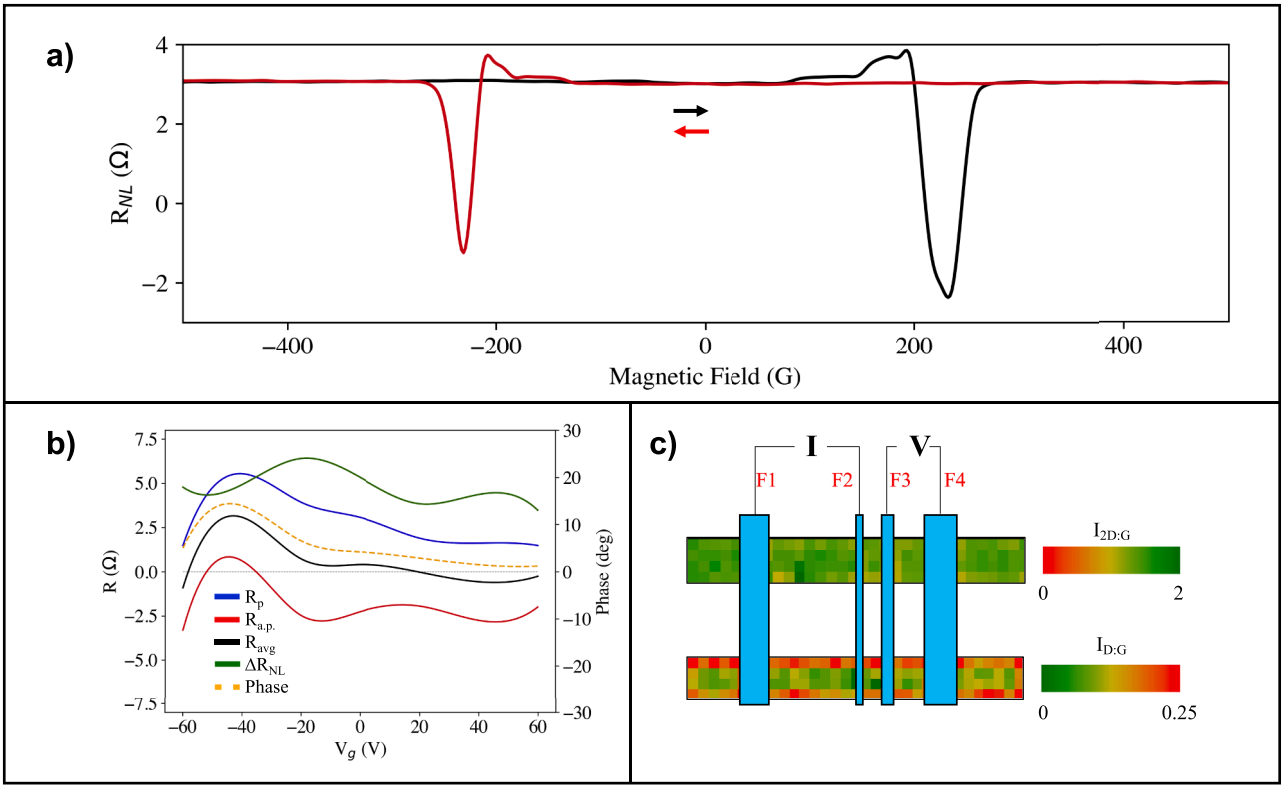

Fig. 4. Experimental results for a device with good tunnel barrier integrity and undamaged channel graphene. (a) Non-local resistance versus magnetic field strength, sweeping toward positive (black) and negative (red) field strengths. (b) Parallel magnetization resistance (R_p), anti-parallel magnetization resistance ($R_{a.p.}$), average of R_p and $R_{a.p.}$ (R_{avg}), spin signal (ΔR_{NL}), and phase angle versus backgate voltage (V_g). (c) 2D:G intensity ratio (upper) and D:G intensity ratio (lower) Raman spectroscopy maps of the device's graphene channel.

2.2. NLSV spintronic and electronic measurements

To evaluate the performance of each individual NLSV, measurements on the array were conducted in a Lakeshore Cryogenic Probe Station at room temperature under vacuum ($\sim 5 \times 10^{-6}$ Torr) using low-frequency ac lock-in techniques. A constant 10 μA current with a 13 Hz carrier frequency was injected into the NLSV current loop via a Keithley 6221 current source. The non-local voltage was detected with a Stanford Research Systems SR850 lock-in amplifier. The magnetic field was parallel to the electrodes on the devices and was swept between +/- 950 Gauss in both directions as the voltage was simultaneously measured using a custom automated interface. All standard electrical measurements, including IV curves and gate sweeps, were conducted using an Agilent B1500A semiconductor parameter analyzer.

2.3. Raman spectroscopy

Raman spectra were collected using a Horiba HR800 UV with a 100 mW, 532 nm excitation laser to determine the quality of the NLSV device channels after completion of electronic and spintronic measurements. Raman maps were collected using the same instrument while moving the piezo stage in 0.5 μm increments for each collection point.

3. Results and discussion

3.1. Graphene characterization

It was first necessary to establish a baseline understanding of the quality of the graphene used to construct the NLSV devices. Investigation of the pre-processed graphene film with optical microscopy revealed drastic variation across the surface, as seen in Fig. 1a. In this field of view, a network of grain boundaries can be observed, with grains having a diameter of 40 to 100 μm. Many bi-layer adlayers are also present, with most having diameters between 5 and 15 μm. The darker spots on some bi-layer adlayers are indicative of a third layer of graphene in those regions. The variation in size of adlayers and grain boundaries is a result of the CVD nucleation growth mechanism [36]. The area within the dashed box in Fig. 1a was mapped using Raman spectroscopy, with the results shown in Fig. 1b–d. Fig. 1b shows a map of the ratio of the 2D peak intensity to the G peak intensity ($I_{2D:G}$) of the graphene spectra. This ratio provides information about graphene layer number, where $I_{2D:G} > 1$ indicates monolayer graphene and $I_{2D:G} < 1$ indicates multilayer graphene [37,38]. Fig. 1c is a map of the ratio of the D peak intensity to the G peak intensity ($I_{D:G}$). This ratio provides information about defect density, where a higher $I_{D:G}$ correlates to more defective graphene [37,39]. For pristine graphene, $I_{D:G} \sim 0$. Fig. 1d displays a map of the location of the 2D peak in the spectrum. Deviation of the 2D peak location from its standard value (~ 2690 cm^{-1}) is characteristic of doping or straining of the graphene [39]. Fig. 1e shows sample Raman spectra from distinct areas within the graphene map: pristine monolayer graphene, graphene adjacent to a grain boundary, and graphene in an adlayer zone. Pristine monolayer graphene tends to have a high $I_{2D:G}$ and low $I_{D:G}$, and a 2D peak that occurs at a lower wavenumber (below ~ 2690 cm^{-1}). Grain boundary graphene can be identified by an increased $I_{D:G}$, a decreased $I_{2D:G}$, and a shift of the 2D peak location to a higher wavenumber (above ~ 2690 cm^{-1}). Adlayer graphene has an even lower $I_{2D:G}$ and an even further shifted 2D peak location than grain boundary graphene, but its D peak remains absent signaling a lack of defects in the graphene lattice.

The interface between the metal electrodes and the graphene channel can have a dramatic impact on the spin signal observed in NLSVs. Five transmission line method (TLM) devices were included on the device array to study the contact resistance of the electrodes with tunnel barriers. These devices contain multiple electrodes separated by varying

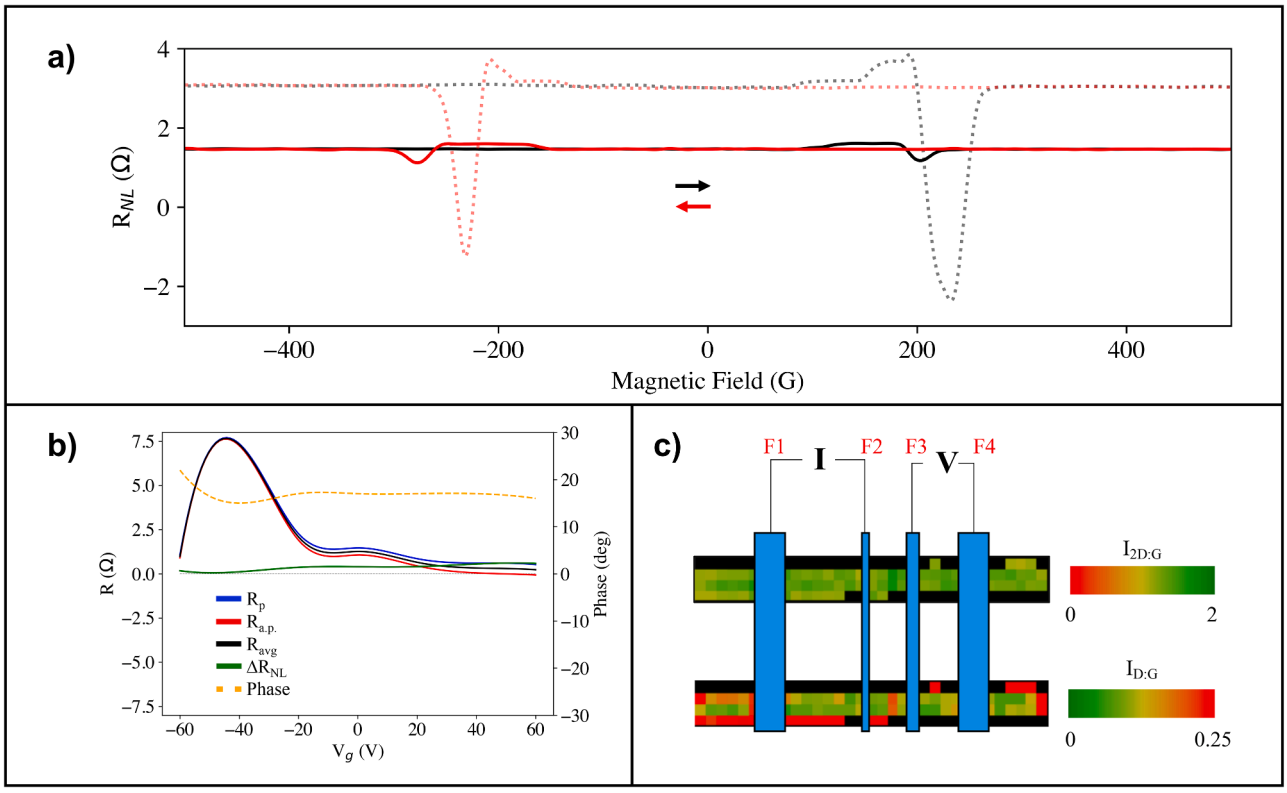

Fig. 5. Experimental results for a device with poor tunnel barrier integrity and undamaged channel graphene. (a) Non-local resistance versus magnetic field strength, sweeping toward positive (black) and negative (red) field strengths, spin signals from Fig. 4 are overlayed as dotted lines. (b) Parallel magnetization resistance (R_p), anti-parallel magnetization resistance ($R_{a.p.}$), average of R_p and $R_{a.p.}$ (R_{avg}), spin signal (ΔR_{NL}), and phase angle versus backgate voltage (V_g). (c) 2D:G intensity ratio (upper) and D:G intensity ratio (lower) Raman spectroscopy maps of the device's graphene channel.

distances that allow for extraction of the contact resistance of the electrodes as well as the sheet resistance of the channel material, as demonstrated in previous literature [40,41]. Here, the graphene channel has a width of 2 μm and the electrodes have a lateral thickness of 500 nm to minimize current crowding effects. Fig. 2a shows the I-V curves for each of the five electrode separations on a single graphene TLM device, showing a linear Ohmic response. If the electrodes were truly tunneling, one would expect non-linear (Schottky-like) I-V curves [42]. Although Schottky contacts are preferable for spintronic applications due to their ability to block spin back-propagation into the injection electrode, Ohmic contacts have been shown to exhibit strong spintronic signal as well [43,44]. The inverse slope of the I-V curve provides the resistance of the entire circuit between any two electrodes (R_{tot}). Plotting this value versus contact spacing, as in Fig. 2b, demonstrates their linear relationship. This relationship is defined by the equation $R_{tot} = R_S{*}d/W_{ch} + 2R_C$, where R_S is the sheet resistance of the graphene, d is the distance between electrodes, W_{ch} is the channel width (in this case, 2 μm), and R_C is the contact resistance [40]. Using the linear fit equation noted in Fig. 2b gives R_C ~2.94 kΩ and R_S ~1.31 kΩ for TLM structures with Co/TiO_2 electrodes and CVD graphene channels with randomly distributed defects as outlined in Fig. 1a.

Fig. 2c shows the effect of sweeping the backgate voltage on sheet resistance (R_S), contact resistance (R_C), and measured total resistance $R_{tot} \sim (L_{ch}/W_{ch}){*}R_S + 2R_C$, where L_{ch} and W_{ch} are the length and width of the graphene channel respectively. The total resistance and sheet resistance curves show the Dirac point occurring at roughly −35 V, indicating n-type doped graphene. There is also a slight shoulder on the total resistance curve at ~0 V, which coincides with a peak in the contact resistance curve. This implies that there is a level of work function pinning in the graphene under the electrodes, indicating that there is direct Co-graphene contact through the tunnel barrier, likely in the form of pinholes [45]. Fig. 2d shows optical micrographs of 40 μm by 40 μm Van der Pauw squares and clovers used to calculate sheet resistance [46]. Defects (adlayers and grain boundaries) are visible in all four devices, leading to their correspondingly higher sheet resistance values than the smaller 2 μm by 16 μm TLMs.

3.2. NLSV devices

A model of the basic NLSV device used in this study is shown in Fig. 3a. A current is injected between ferromagnetic electrodes F1 and F2 (I_{inj}). Charge current exists between F2 and F1, and spin current propagates out from F2 toward both F1 and F3. In an ideal device, only pure spin current, and no charge current, will exist between F2 and F3. This is due to an accumulated spin imbalance that is created under F2 that diffuses toward F3. Electrodes F2 and F3 are separated by a distance Δx. The accumulation of a spin imbalance beneath F3 changes its chemical potential compared to the reference electrode F4, resulting in a measurable voltage between the two electrodes (V_{det}). Fig. 3b shows a detailed example of a R_{NL} versus magnetic field sweep measurement. Here, three distinct R_{NL} levels can be identified based on the magnetic polarization of the electrodes F2, F3, and F4. The F1 electrode is further away from the current injection region, and so its effects on R_{NL} are minimal.

The device array contained 20 NLSV devices (ten where $\Delta x = 1$ μm, ten where $\Delta x = 2$ μm). Of these 20, only 15 had observable spin signal (nine where $\Delta x = 1$ μm, six where $\Delta x = 2$ μm). The most common failure mode was a broken 200 nm wide injector electrode (F2). Statistics for several parameters are outlined in Table 1.

The change in magnitude of the non-local resistance between the parallel (R_p) and anti-parallel ($R_{a.p.}$) magnetization polarization of electrodes F2 and F3 (spin signal, ΔR_{NL}) is a critical indicator of device quality. This value is dependent on the integrity of the graphene-electrode interface, with better resistance matching typically

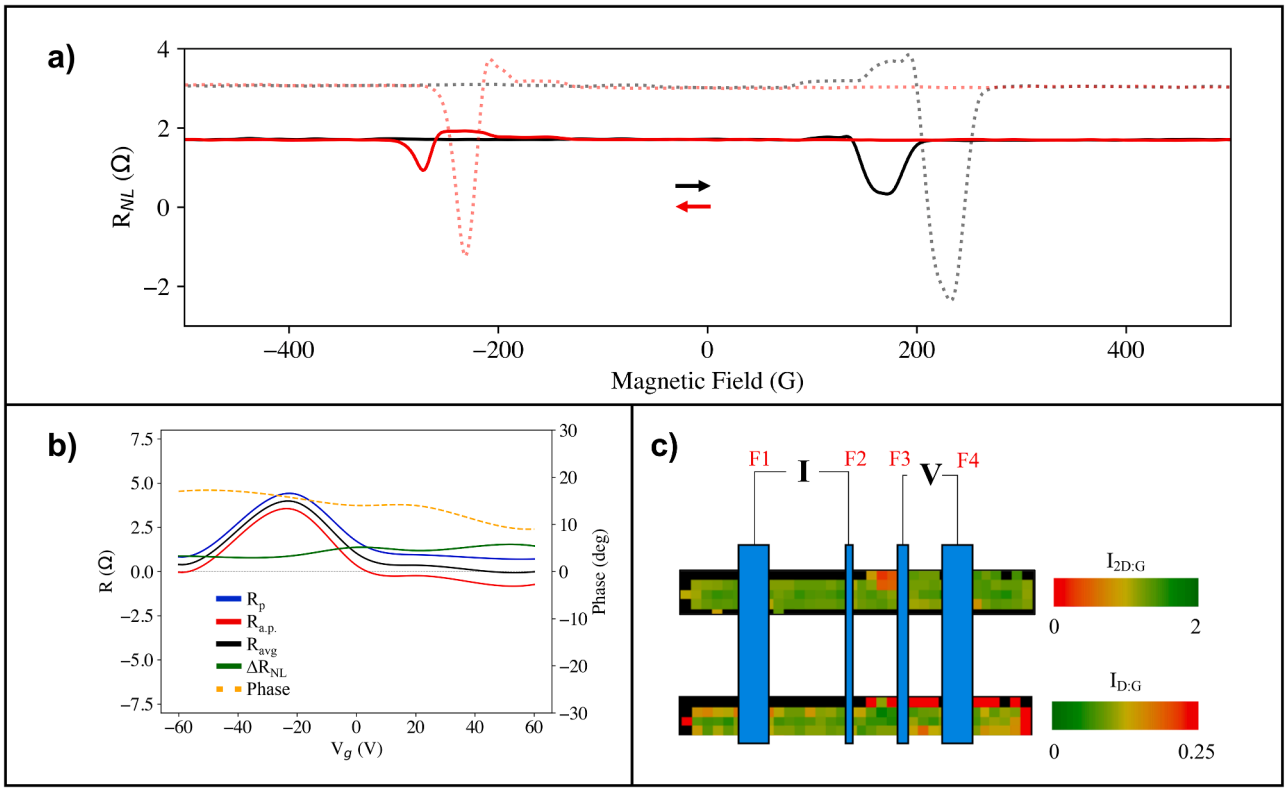

Fig. 6. Experimental results for a device with poor tunnel barrier integrity and a channel containing an adlayer between electrodes F2 and F3. (a) Non-local resistance versus magnetic field strength, sweeping toward positive (black) and negative (red) field strengths, spin signals from Fig. 4 are overlayed as dotted lines. (b) Parallel magnetization resistance (R_p), anti-parallel magnetization resistance ($R_{a.p.}$), average of R_p and $R_{a.p.}$ (R_{avg}), spin signal (ΔR_{NL}), and phase angle versus backgate voltage (V_g). (c) 2D:G intensity ratio (upper) and D:G intensity ratio (lower) Raman spectroscopy maps of the device's graphene channel.

providing larger ΔR_{NL}. The median ΔR_{NL} value for the 1 μm and 2 μm channel devices were both just under 1 Ω, however several high-value outliers in the 1 μm devices result in a much higher standard deviation. These outliers that possess large ΔR_{NL} are the result of minimal charge current between the injector and detector electrodes as a result of higher quality tunnel barrier layers on these devices. The phase shift of the detected voltage as measured by the lock-in amplifier varies more in the 1 μm devices than in the 2 μm devices, although both electrode configurations have relatively high median phase shift. Phase shift away from 0° (i.e., where all signal resides in the "X" channel of the lock-in amplifier) can be an indicator of charge current between F2 and F3, as opposed to the ideal case of pure spin current only [47]. The location of the charge neutrality point (Dirac point) as measured by a backgate sweep between electrodes F1 and F4 was relatively consistent across devices at around −35 V, indicating n-type doping potentially arising from the SiO2 substrate, or charged impurities on the surface [48,49].

Magnetic sweep measurements and micro-Raman spectroscopy mapping were performed on each device to assess spin transport capabilities, contact quality, and channel material quality. Experimental results from a device with pristine graphene quality are shown in Fig. 4. As seen in the magnetic sweep data of Fig. 4a, the value of ΔR_{NL} is ~5 Ω with a near full sign reversal of the non-local resistance in the anti-parallel state. This is indicative of good conductivity matching between the electrodes and the graphene channel, which minimizes spin backflow into the injector and allows for a higher level of spin-polarized current to flow to the detector electrode. The large spin imbalance then leads to spin diffusion across the graphene channel and results in a large voltage differential at the detector electrode. The quality of the contacts is further investigated in Fig. 4b, where magnetic sweeps were conducted over a range of backgate voltages (V_g). There is an observable peak in the parallel and anti-parallel resistances near the Dirac point, as well as a peak in the phase shift. Away from the Dirac point, the average of the parallel and anti-parallel resistances remains close to 0, indicating that the two states have nearly equal and opposite resistance values as is ideal for a pure spin signal [50]. The phase shift also trends toward 0 away from the Dirac point, indicating that the effect of charge current on ΔR_{NL} is reduced [47]. The magnitude of ΔR_{NL} stays above 2.5 Ω across the V_g spectrum. These factors indicate that, while there is still some charge current present between the injector and detector electrodes, the effect of the pure spin current is much stronger. Fig. 4c shows Raman spectroscopy maps of the graphene channel. The entire channel has a 2D:G peak intensity ratio ($I_{2D:G}$) of >1, indicating monolayer graphene throughout. The D:G peak intensity ratio ($I_{D:G}$) of the center of the channel is <0.1, indicating a lack of damage to the graphene structure. The edges of the channel have higher $I_{D:G}$, which is indicative of damage due to the plasma etching process used for channel definition.

Fig. 5 presents experimental data from a device also possessing a pristine graphene channel, but with poorer electrode performance. The magnetic sweep shown in Fig. 5a indicates lower non-local spin signal than the device analyzed in Fig. 4. In this device the non-local resistance does not exhibit sign inversion and ΔR_{NL} is only ~1.2 Ω, indicating poor spin injection or detection. Analysis of the non-local resistance values, spin signal, and phase versus backgate voltage in Fig. 5b indicates poor electrode performance. The phase angle oscillates around 15°, indicating that there is charge current between the injector and detector electrodes. Furthermore, R_p and $R_{a.p.}$ are close together throughout the backgate sweep yielding a low ΔR_{NL}, and $R_{a.p.}$ stays positive until V_g is around 20 V. The average of R_p and $R_{a.p.}$ finally trends to 0 Ω once V_g reaches >40 V. The Raman maps of the channel of this device shown in Fig. 5c present similarly to those in Fig. 4c – a high $I_{2D:G}$ throughout the channel and a low $I_{D:G}$ in the channel center, indicating pristine monolayer graphene.

Fig. 6 shows representative data from a device with an adlayer between the injector and detector electrodes. The adlayer can be observed

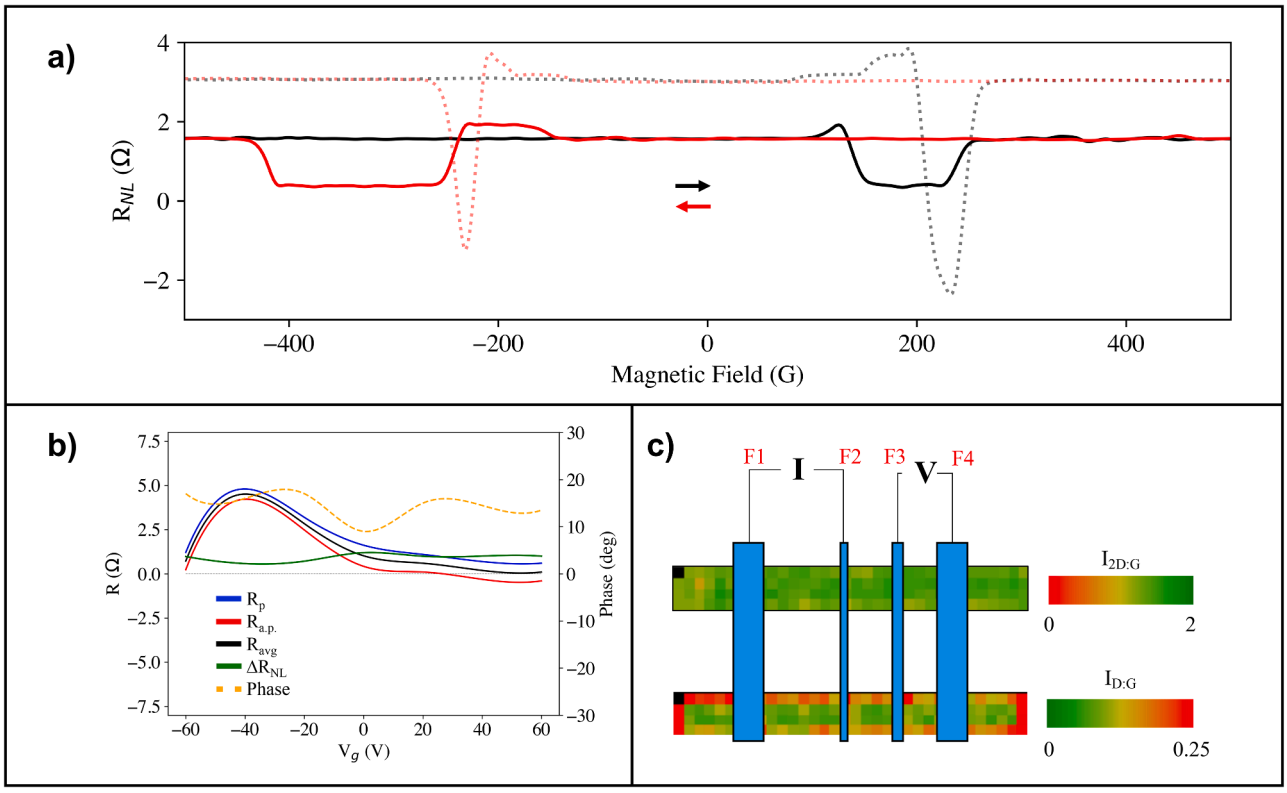

Fig. 7. Experimental results for a device with poor tunnel barrier integrity and a channel with a grain boundary between electrodes F2 and F3. (a) Non-local resistance versus magnetic field strength, sweeping toward positive (black) and negative (red) field strengths, spin signals from Fig. 4 are overlayed as dotted lines. (b) Parallel magnetization resistance (R_p), anti-parallel magnetization resistance ($R_{a.p.}$), average of R_p and $R_{a.p.}$ (R_{avg}), spin signal (ΔR_{NL}), and phase angle versus backgate voltage (V_g). (c) 2D:G intensity ratio (upper) and D:G intensity ratio (lower) Raman spectroscopy maps of the device's graphene channel.

in Fig. 6c as the orange region in the $I_{2D:G}$ map, between electrodes F2 and F3. As seen in Fig. 6a, this device has a ΔR_{NL} value of 1.36 Ω, the highest value recorded for a 2 μm channel length device. Fig. 6b shows how the non-local resistance measurements and phase change with V_g. The phase of the non-local signal stays between 10 and 20°, indicating that there is some charge current present between the injector and detector electrodes, however R_{avg} trends toward 0 Ω at higher V_g. This indicates that the presence of the adlayer within the spin transport region does not negatively impact the spin signal.

Fig. 7 shows representative data from a device with a damaged graphene channel. Although the $I_{2D:G}$ map, as shown in Fig. 7c, shows monolayer graphene, the $I_{D:G}$ map shows a defect line running directly between the injector and detector electrodes. Further optical microscopy inspection revealed a grain boundary running through this region of the channel. As this is the region where pure spin transport in the device occurs, it is expected that this grain boundary would act as a spin scattering site. This is confirmed by the magnetic sweep data shown in Fig. 7a, where ΔR_{NL} is observed to be ~0.27 Ω. The impact of V_g on phase and non-local resistance in this device, as seen in Fig. 7b, indicates that charge current dominates the signal to a higher degree than in the devices profiled in Figs. 5 and 6.

Overall, the proportion of devices negatively impacted by graphene defects such as grain boundaries and adlayers is relatively low. This is, in part, due to the small dimensions of the channels. Adlayers within the channel area do not appear to have a negative effect on the spin signal, likely due to the ability of spin transport to occur exclusively within the first layer of graphene that is contacted by the electrodes. The Raman data in Fig. 1c and e show that these adlayers do not present areas with increased defects, indicating that the crystal lattice is not damaged. Grain boundaries, on the other hand, appear to reduce ΔR_{NL} by ~75 % when they occur between the injector and detector electrodes. This is likely caused by spin dephasing occurring at the boundary due to discontinuity of the graphene crystal lattice. Due to the small surface area of the graphene channel (~22 μm^2 for these devices) compared to the average grain size of the CVD graphene sheets (~1250–7800 μm^2), the occurrence of grain boundaries running through the channels is fairly low. However, as spintronic architectures grow more complex, channel lengths will need extend to connect neighboring devices, necessitating improved CVD processes for reduced grain boundary density. In contrast to intrinsic graphene sheet properties, tunneling contact quality has a far greater impact on device variability. Both the transfer mechanism during initial CVD processing, as well as the multiple e-beam lithography steps during patterning result in a graphene sheet laden with PMMA particles varying from several nanometers to several microns in diameter. These particles play a major role in disrupting the tunneling characteristics of the contacts, introducing undesirable charge transport into the NLSVs where the Co layer directly interfaces with the graphene sheet. These particles are randomly distributed, and so contribute greatly to the variance between identical devices on the same array. Methods for enhanced cleaning of PMMA from graphene, or its exclusion from the process flow entirely, will be crucial for fabrication of consistent graphene spintronic devices.

4. Conclusion

In summary, the results presented in this work help to shed light on the feasibility of fabricating spintronic devices with consistent properties on commercially available wafer-scale CVD graphene. Through analysis of this device array, the impact of graphene inhomogeneity and contact variability have been assessed. It has been shown that devices of identical form factor have high variability across the same array. Adlayer regions commonly present on CVD graphene samples appear to have minimal negative effect on spin signal, however grain boundaries in the spin transport region of non-local spin valves act as spin scattering

sources that lead to a reduction of ΔR_{NL}. It has also been demonstrated that variability of contact quality has a major impact on device consistency, likely due to pinholes in the tunnel barrier layer of the electrodes. These findings help to shape a path forward for what must be improved prior to reliable fabrication of wafer-scale graphene spintronic devices.

Declaration of Competing Interest

The authors declare that they have no known competing financial interests or personal relationships that could have appeared to influence the work reported in this paper.

Data availability

Data will be made available on request.

Acknowledgments

This research is funded by the National Science Foundation (NSF) award No. 1711994, and by funds from the Oregon Metals Initiative (OMI). The electron beam lithography processes for the designed NLSVs arrays were performed at Notre Dame Nanofabrication Facility (NDNF), University of Notre Dame.

References

[1] S. Patil, et al., Spintronic logic gates for spintronic data using magnetic tunnel junctions, in: Proceedings of the 2010 IEEE International Conference on Computer Design, 2010. IEEE.
[2] J.S. Friedman, et al., Cascaded spintronic logic with low-dimensional carbon, Nat. Commun. 8 (1) (2017) 15635.
[3] E.C. Ahn, 2D materials for spintronic devices, Npj 2D Mater. Appl. 4 (1) (2020) 17.
[4] R. Jansen, The spin-valve transistor: a review and outlook, J. Phys. D Appl. Phys. 36 (19) (2003) R289.
[5] Y. Ji, et al., Spin injection, diffusion, and detection in lateral spin-valves, Appl. Phys. Lett. 85 (25) (2004) 6218–6220.
[6] J.Q. Xiao, J.S. Jiang, C.L. Chien, Giant magnetoresistance in nonmultilayer magnetic systems, Phys. Rev. Lett. 68 (25) (1992) 3749.
[7] Y. Ji, et al., Non-local spin injection in lateral spin valves, J. Phys. D Appl. Phys. 40 (5) (2007) 1280.
[8] E. Villamor, et al., Contribution of defects to the spin relaxation in copper nanowires, Phys. Rev. B 87 (9) (2013), 094417.
[9] D. Kochan, M. Gmitra, J. Fabian, Spin relaxation mechanism in graphene: resonant scattering by magnetic impurities, Phys. Rev. Lett. 112 (11) (2014), 116602.
[10] W. Han, et al., Graphene spintronics, Nat. Nanotechnol. 9 (10) (2014) 794–807.
[11] A. Avsar, et al., Colloquium: spintronics in graphene and other two-dimensional materials, Rev. Mod. Phys. 92 (2) (2020), 021003.
[12] P. Seneor, et al., Spintronics with graphene, MRS Bull. 37 (12) (2012) 1245–1254.
[13] W. Yan, et al., Long spin diffusion length in few-layer graphene flakes, Phys. Rev. Lett. 117 (14) (2016), 147201.
[14] W. Han, et al., Spin transport and relaxation in graphene, J. Magn. Magn. Mater. 324 (4) (2012) 369–381.
[15] K.S Novoselov, et al., Electric field effect in atomically thin carbon films, science 306 (5696) (2004) 666–669.
[16] Y.I. Zhang, L. Zhang, C. Zhou, Review of chemical vapor deposition of graphene and related applications, Acc. Chem. Res. 46 (10) (2013) 2329–2339.
[17] X. Wang, et al., The transition metal surface dependent methane decomposition in graphene chemical vapor deposition growth, Nanoscale 9 (32) (2017) 11584–11589.
[18] I. Vlassiouk, et al., Role of hydrogen in chemical vapor deposition growth of large single-crystal graphene, ACS Nano 5 (7) (2011) 6069–6076.
[19] Z. Yan, Z. Peng, JM. Tour, Chemical vapor deposition of graphene single crystals, Acc. Chem. Res. 47 (4) (2014) 1327–1337.
[20] G. Nandamuri, S. Roumimov, R. Solanki, Chemical vapor deposition of graphene films, Nanotechnology 21 (14) (2010), 145604.
[21] M. Her, R. Beams, L. Novotny, Graphene transfer with reduced residue, Phys. Lett. A 377 (21–22) (2013) 1455–1458.
[22] LP. Biró, P. Lambin, Grain boundaries in graphene grown by chemical vapor deposition, New J. Phys. 15 (3) (2013), 035024.
[23] A.W. Tsen, et al., Polycrystallinity and stacking in CVD graphene, Acc. Chem. Res. 46 (10) (2013) 2286–2296.
[24] K. Kim, et al., Grain boundary mapping in polycrystalline graphene, ACS Nano 5 (3) (2011) 2142–2146.
[25] J. Kang, et al., Graphene transfer: key for applications, Nanoscale 4 (18) (2012) 5527–5537.
[26] G. Deokar, et al., Towards high quality CVD graphene growth and transfer, Carbon 89 (2015) 82–92. N Y.
[27] S. Ullah, et al., Graphene transfer methods: a review, Nano Res. (2021) 1–17.
[28] V. Kochat, et al., Magnitude and origin of electrical noise at individual grain boundaries in graphene, Nano Lett. 16 (1) (2016) 562–567.
[29] Q. Yu, et al., Control and characterization of individual grains and grain boundaries in graphene grown by chemical vapour deposition, Nat. Mater. 10 (6) (2011) 443–449.
[30] G. Fiori, et al., Bilayer graphene transistors for analog electronics, IEEE Trans. Electron Devices 61 (3) (2014) 729–733.
[31] W. Han, R.K. Kawakami, Spin relaxation in single-layer and bilayer graphene, Phys. Rev. Lett. 107 (4) (2011), 047207.
[32] L. Gammelgaard, et al., Graphene transport properties upon exposure to PMMA processing and heat treatments, 2D Mater. 1 (3) (2014), 035005.
[33] Y.C. Lin, et al., Graphene annealing: how clean can it be? Nano Lett. 12 (1) (2012) 414–419.
[34] A. Pirkle, et al., The effect of chemical residues on the physical and electrical properties of chemical vapor deposited graphene transferred to SiO2, Appl. Phys. Lett. 99 (12) (2011), 122108.
[35] W. Fu, et al., Large-scale fabrication of BN tunnel barriers for graphene spintronics, J. Appl. Phys. 116 (7) (2014), 074306.
[36] M.H. Ani, et al., A critical review on the contributions of chemical and physical factors toward the nucleation and growth of large-area graphene, J. Mater. Sci. 53 (2018) 7095–7111.
[37] A.C. Ferrari, et al., Raman spectrum of graphene and graphene layers, Phys. Rev. Lett. 97 (18) (2006), 187401.
[38] Y. Hao, et al., Probing layer number and stacking order of few-layer graphene by Raman spectroscopy, small 6 (2) (2010) 195–200.
[39] R. Beams, L.G. Cançado, L. Novotny, Raman characterization of defects and dopants in graphene, J. Phys. Condens. Matter 27 (8) (2015), 083002.
[40] S. Russo, et al., Contact resistance in graphene-based devices, Phys. E: Low-Dimens. Syst. Nanostructures 42 (4) (2010) 677–679.
[41] S. Venica, et al., On the adequacy of the transmission line model to describe the graphene–metal contact resistance, IEEE Trans. Electron Devices 65 (4) (2018) 1589–1596.
[42] W. Han, et al., Tunneling spin injection into single layer graphene, Phys. Rev. Lett. 105 (16) (2010), 167202.
[43] W. Han, et al., Electrical detection of spin precession in single layer graphene spin valves with transparent contacts, Appl. Phys. Lett. 94 (22) (2009), 222109.
[44] E.W. Hill, et al., Graphene spin valve devices, IEEE Trans. Magn. 42 (10) (2006) 2694–2696.
[45] S.M. Song, B.J. Cho, Contact resistance in graphene channel transistors, Carbon Lett. 14 (3) (2013) 162–170.
[46] L.J. Van der Pauw, A method of measuring specific resistivity and Hall effect of discs of arbitrary shape, Philips Res. Rep. 13 (1) (1958) 1–9.
[47] F. Volmer, et al., Charge-induced artifacts in nonlocal spin-transport measurements: how to prevent spurious voltage signals, Phys. Rev. Appl. 18 (1) (2022), 014028.
[48] J.H. Chen, et al., Charged-impurity scattering in graphene, Nat. Phys. 4 (5) (2008) 377–381.
[49] H.E. Romero, et al., N-type behavior of graphene supported on Si/SiO2 substrates, ACS Nano 2 (10) (2008) 2037–2044.
[50] S. Cho, Y.F. Chen, M.S. Fuhrer, Gate-tunable graphene spin valve, Appl. Phys. Lett. 91 (12) (2007), 123105.